PCCP

ROYAL SOCIETY OF CHEMISTRY

PERSPECTIVE

View Article Online
View Journal | View Issue

Cite this: *Phys. Chem. Chem. Phys.*, 2023, **25**, 27926

Theoretical approaches to defect mechanisms and transport properties of compounds used for electrodes and solid-state electrolytes in alkali-ion batteries†

Yohandys A. Zulueta [a] and Minh Tho Nguyen *[bc]

Received 29th July 2023,
Accepted 26th September 2023

DOI: 10.1039/d3cp03627h

rsc.li/pccp

The transition from fossil fuels to cleaner energies employing different renewable sources constitutes one of the primary worldwide challenges. The search for appropriate solutions is becoming more urgent in view of the severe consequences of climate change. As for a perspective, stationary energy storage, alkali-ion batteries and hybrid supercapacitors are, among others, considered as efficient and affordable solutions. Alkali-ion batteries have proved to be the most investigated products in the past decade including optimizations for cost, energy density and safety. In this Perspective, a computational approach and its applicability in the inverse material design are presented. This approach includes density functional theory calculations, force field-based determinations and both static and molecular dynamics simulations. As for an illustration, the main properties of a selected series of battery materials, including oxides and sulfides Li_2SiO_3, Li_2SnO_3, $SrSnO_3$, and $A_2B_6X_{13}$ (A = Li^+, Na^+, K^+; B = Ti^{4+}, Sn^{4+}; X = O^{2-}, S^{2-}), and mixed halide antiperovskite A_3OX (A = Li^+, Na^+; X = Cl^-, Br^-) are explored in depth using these theoretical approaches. Doping strategies, new dopant incorporation mechanism, treatment with alkali insertion/de-insertion cycle in electrodes, transport properties, as well as thermodynamic stability, are discussed. Theoretical approaches reveal that the oxygen–sulfur exchange in alkali hexatitanates and hexastannates induces remarkable improvement of the required properties for electrode and electrolyte materials. In addition, doping of Li_2SiO_3 with low Na-concentration enhances the room temperature Li-diffusivity by a reduction of the activation energy. The effects of transition-metal and divalent dopants on the defect chemistry and transport properties of Li_2SnO_3 are also disclosed. The interstitial trivalent doping mechanism is a friendly synthesis strategy to improve the large-scale diffusion in Li_2SnO_3. The potential of $SrSnO_3$ as an anode in alkali-ion batteries, and the influence of a particular grain boundary in nanocrystalline antiperovskite A_3OX are also revealed by using advanced atomistic simulations. The computational approaches described here provide us with a convenient tool for the determination of the properties of battery materials with high accuracy and for the prediction of characteristics of a new generation of alkali battery materials that could be used in improved technologies.

1. Introduction

For a successful use as an electrode and electrolyte in an alkali-ion battery, the material should satisfy specific requirements, some of those key requirements are common for both the electrode and the electrolyte.[1–13] The principal prerequisites for a material to be considered as a main component of a rechargeable alkali-ion battery are: the material (a) contains a reducible/oxidisable ion, such as a transition metal atom (for the positive electrode being called the cathode), (b) has high chemical and mechanical stability, reacting reversibly with the alkali-ion with a minimal structural change upon insertion/extraction of the alkali-ion leading to good cycle life, (c) has excellent electronic and alkali-ion conductivity facilitating the electrochemical reaction, (d) accommodates several alkali-ions per metallic alkali in order to provide high capacity and energy density, (e) having a high voltage for the cathode ($\approx$4 V) and a low voltage for the anode ($\approx$0.5 V) to satisfy the 5 V electrochemical window for the electrolyte stability, and (f) low cost and environmentally benign. In addition, the solid-state

[a] *Departamento de Física, Facultad de Ciencias Naturales y Exactas, Universidad de Oriente, CP-90500, Santiago de Cuba, Cuba*
[b] *Laboratory for Chemical Computation and Modeling, Institute for Computational Science and Artificial Intelligence, Van Lang University, Ho Chi Minh City, Vietnam. E-mail: minhtho.nguyen@vlu.edu.vn*
[c] *Faculty of Applied Technology, School of Technology, Van Lang University, Ho Chi Minh City, Vietnam*

† Electronic supplementary information (ESI) available. See DOI: https://doi.org/10.1039/d3cp03627h

electrolyte must be malleable (having a reasonably small Young's Modulus and being mechanically stable), ensuring good contact with the electrodes, and possessing insulating electronic characteristics to avoid reactions with the electrodes which cause undesirable alkali loss during the charge/discharge process, dendrite formation and high electronic conductivity through the electrolyte (producing possible short-circuit).[1–13] Throughout this paper, a material with a potential application as an electrode (either a cathode or an anode) and an electrolyte, as well as a coating electrode, is labelled a battery material.

As for the anode, a comprehensive evaluation of its performance is still needed to select the best candidate material.[14–16] For instance, carbon-based anodes have a specific capacitance lower by a factor of 10 compared to alkali-containing anodes.[14–16] Lithium titanium oxide ($Li_4Ti_5O_{12}$) remains the most commonly used Li-containing anode due to its relatively high ionic conductivity at operating temperatures and zero-stain upon cycling.[15,17]

On the other hand, sulfide-containing compounds have been shown to be potentially suitable for energy storage applications.[18–21] The advantages of this class of compounds are that they behave as better ionic conductors and are deformable compared to their oxygen-containing counterparts. Their intrinsic deformability allows better contact between the electrode and the electrolyte and reduces grain boundary resistance.[18–24] Of particular interest are the alkali hexatitanates, which have a tunnel structure responsible for their key physicochemical properties.[1–4,25–28]

Several studies have been devoted to the improvement of different properties of battery materials. The most popular method used for such a purpose consists of a compositional modification of the lattice structure upon creation of ionizable species within the compound thereby leading to free mobile charge carriers. This concept is well known as doping.[29,30] Various synthesis methods have been designed for doping and tuning the charge carrier concentration in the sample.[30–33] A majority of these experimental methods are rather expensive, especially for research groups from developing countries. Therefore, advanced atomistic simulations can help the experimentalists to select appropriate dopants to improve a particular property, alleviating negative effects.[1–10,22,23]

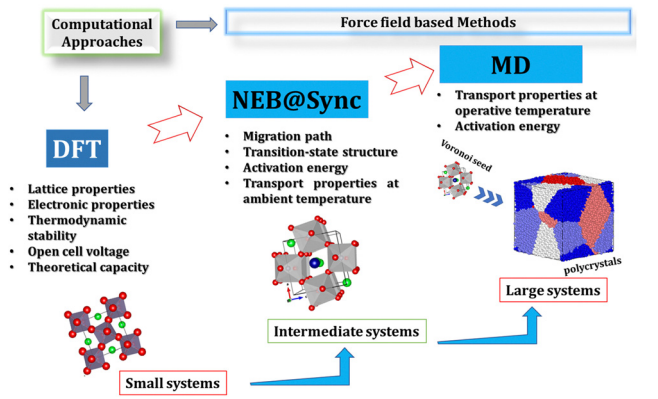

Fig. 1 Integrated computational approaches.

This manuscript is devoted to a review of our recent advances in the design of selected battery materials. The structural and electronic properties, thermodynamic stability, defect chemistry and transport properties of a series of compounds, including Li_2SnO_3, Li_2SiO_3, $SrSnO_3$, $A_2B_6X_{13}$ (A = Li^+, Na^+, or K^+; B = Ti^{4+} or Sn^{4+}; X = O^{2-} or S^{2-}) and alkali–halide oxides A_3OX (A = Li, Na, X = Cl or Br), are explored employing advanced atomistic simulations. A clear description of the computational protocols used for atomistic simulations is essential for inverse material design. A number of relevant questions need to be answered in this process, namely, how these computational protocols help the experimentalists in selecting a battery material? What are the precautions to be taken when these computational approaches are used for prediction? How transferable are these computational protocols for predicting the properties of other classes of compounds? In this manuscript, we set out to provide convincing answers, illustrated by our recent work, to these questions. We intend to disseminate these computational protocols as a reasonable tool for exploring the meaning of some main properties of current and future battery materials including their defect mechanisms and transport properties at the molecular level.

2. Computational approaches

The relevance of employing computational approaches in materials design, synthesis strategies and defect engineering investigations has been proven during the development of energy storage devices.[15,22–24] We have used various computational methods to investigate the structural and electronic properties, mechanical and thermodynamic stability, defect formation and migration in relevant battery materials.[1–10] These methods are summarized in the ESI† for disseminating these computational protocols and stimulating their use by the readers.

Fig. 1 displays the computational approaches used in this manuscript. These computational protocols – that are categorized as force field-based and quantum chemical-based methods – include different sets of computations using density functional theory (DFT) computations, static simulations based on the nudged elastic band (NEB), synchronous transition state (Sync), defect energetics computations and large-scale molecular dynamics (MD) simulations. The band structure, density of the states, open cell voltage, and mechanical and thermodynamic stability are properties predicted using DFT computations. Static simulations are used to explore the solution and binding energy of dopants for understanding the defective energetic behavior of a given structure. The NEB method is useful for studying the migration path and evaluating the transport properties at different temperatures. The MD protocol is mainly used to disclose the alkali transport properties for large systems with defect engineering included. In what follows, applications of these protocols to a selection of battery materials are discussed in detail.

Let us stress again that the primary aim of this paper is to share our computational approaches, protocols and experience in identifying the key properties of battery materials and their potential transferability to the theoretical study of other types

of solid-state compounds. The sections of the present paper describe in some detail the findings from our computational protocols, as outlined in the ESI† file, through a series of case studies. Each section provides a comprehensive analysis and discussion of the physicochemical properties of the compounds investigated. In each case study, we emphasize the particular computational methods utilized and the corresponding properties determined from them.

3. Selected case studies

3.1 Disclosing the effect of oxygen–sulfur exchange on the relevant properties of alkali-metal hexastannates and hexatitanates employing DFT computations

Alkali hexatitanates $A_2Ti_6O_{13}$, with A = Li^+, Na^+ or K^+, exhibit a tunnel structure facilitating the intercalation of alkali-ions.[3,4,28–32] These compounds can accommodate about three alkali-ions per formula unit in the potential range of 0.9–1.5 V.[3,4,28–32] Sulfur-containing compounds have been shown to have better ionic conductors and deformability.[11,21,22] Taking advantage of both sulfur-containing compounds and $A_2Ti_6O_{13}$ tunneled structures, we explored relevant properties of $A_2B_6X_{13}$ with A = Li^+, Na^+ or K^+; B = Ti^{4+} or Sn^{4+} and X = O^{2-} or S^{2-} compounds.

New battery materials can be obtained by simple full substitution of one host ion by another with the same valence charge; this method is known as the ion exchange. Fig. 2(a) includes two specific ion exchange cases, with the aim of obtaining $Na_2Ti_6X_{13}$ from $Li_2Ti_6X_{13}$ *via* Na/Li ion exchange, and the second example results in $A_2Sn_6X_{13}$ from their $A_2Ti_6X_{13}$ counterpart *via* Sn/Ti ion exchange. Following the DFT protocol described in the ESI† file, DFT computations were carried out to determine their respective ground state properties.[3,4] The designed monoclinic $A_2B_6X_{13}$ structure contains an array of three zig-zag [BX_6] octahedral sharing edges forming a chain (*cf.* Fig. 2(a)).[3,4,28–30] The results regarding the variation of the lattice parameter show that O^{2-}/S^{2-} exchange induces expansion of the cell parameters, reducing the β angle as compared to their oxygen-containing counterpart.[3,4] Such a change in the cell parameters is a direct consequence of the ion exchange.[3,4]

Fig. 2(b) and (c) depict the energy gap (E_g) values of $A_2B_6X_{13}$ structures derived from various exchange functionals within the generalized gradient approximation (GGA),[3,4] including the Perdew, Burke and Ernzerhof (PBE), Revised Perdew, Burke and Ernzerhof (RPBE), Perdew–Wang (PW91) and PBE with Wu-Cohen (WC). The predicted sulfur $A_2Sn_6S_{13}$ materials have smaller E_g values as compared to their oxygen $A_2Sn_6O_{13}$ counterparts. $A_2Sn_6X_{13}$ are semiconductors in which $K_2Sn_6S_{13}$ has the smallest E_g value. The new sulfur compounds $A_2Ti_6S_{13}$ have smaller E_g values (*cf.* Fig. 2(c)). The metallic character is emphasized for $Li_2Ti_6S_{13}$ and $K_2Ti_6S_{13}$, making these sulfur compounds promising electrode materials.

Tables S1 and S2 provided in the ESI† file show that all of these compounds are stable with respect to decomposition processes.[1,3,4] Furthermore, the values of decomposition

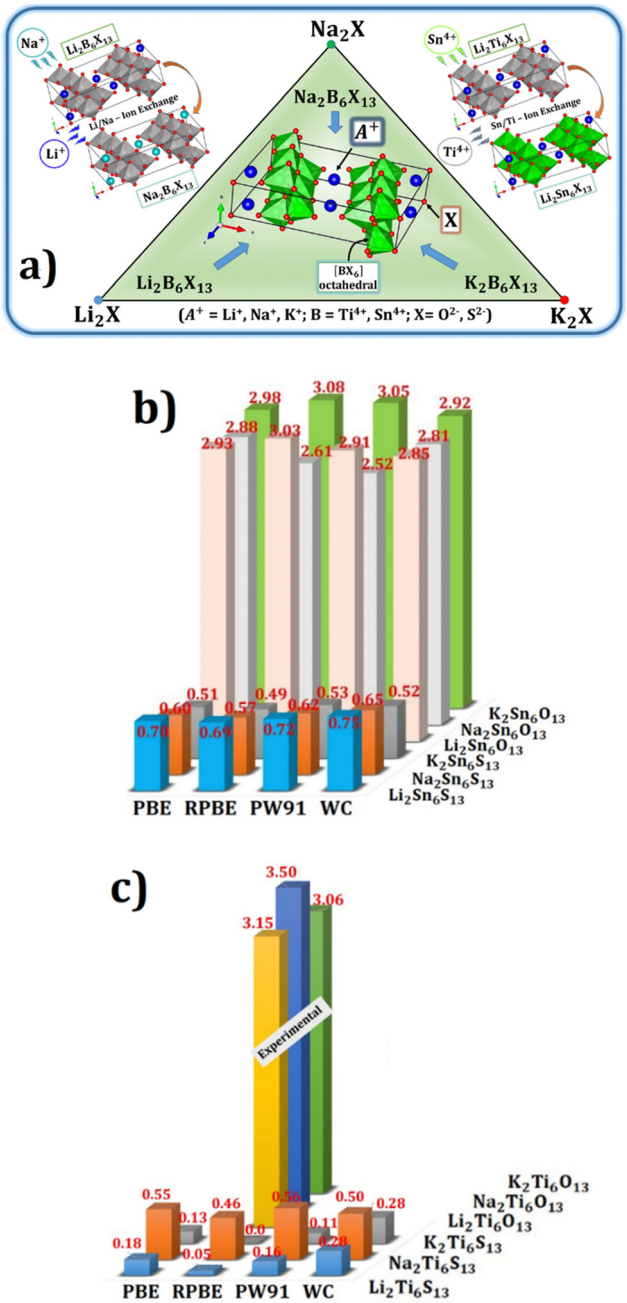

Fig. 2 (a) Outline representation of the $A_2B_6X_{13}$ structures. The figure inset shows the conventional cell of the $A_2B_6X_{13}$ structures and the ion exchange methods. Band gaps (in eV) of (b) $A_2Sn_6X_{13}$ and (c) $A_2Ti_6X_{13}$ structures calculated using different functionals. Experimental values of $A_2Ti_6O_{13}$ are included in (c) for comparison.

reaction energy of the alkali-ions are the lowest ones,[1,3,4] implying that the alkali-ion comprises the charge and mass carriers responsible for the overall transport properties in these compounds. These results reveal the ability by which the alkali-ion exchange occurs during the synthesis, suggesting a real possibility of the formation of these new compounds.

In view of their energy gap, $A_2B_6O_{13}$ oxides remain as semiconductors, whereas $A_2B_6S_{13}$ sulfides take on accentuated metallic character. A comparison of the electronic properties

and stability points out that the O^{2-}/S^{2-} ion-exchange results in better electronic properties and higher thermodynamic stability for $A_2B_6S_{13}$ structures.[3,4] The open cell voltage ranges between the values previously reported for known battery materials.[3,4,17–19] In summary, the oxygen–sulfur exchange in alkali hexatitanates and hexastannates improves the required properties for battery materials.

3.2 Combining lattice static simulations with MD computations for evaluation of Li_2SiO_3 as an inorganic solid electrolyte

The solid-state electrolyte is the other important component in energy storage devices. Of particular interest, we used the computational protocol exposed in the ESI† to explore the Na^+ and K^+ storage proficiency of the lithium silicate Li_2SiO_3 for alkali-ion batteries. Defect energetics of various alkali incorporation mechanisms into the Li_2SiO_3 lattice structure were studied.[5] The first incorporation scheme involves a replacement of alkali leading to no charge defects in defective Li_2SiO_3. The second defect scheme is the Li_2O Schottky defect, which involves two Li vacancies (V'_{Li}) and one oxygen vacancy $(V^{\bullet\bullet}_{O})$ for charge compensation, resulting in a $Li_{2-x}SiO_{3-0.5x}$ sample. The last incorporation mechanism is a combination of these schemes resulting in the formation of $Li_{2-x}Na_xSiO_{3-0.5x}$ and $Li_{2-x}K_xSiO_{3-0.5x}$ samples.[5]

The results of static simulations reveal the favorable incorporation of Na- and K-ions into the Li_2SiO_3 lattice structure.[5] The binding between Li and O vacancies is favorable and reduces the formation energy of Li_2O Schottky defects.[5] Formation of defect clusters is confirmed by binding energy values. Na- and K-doping schemes are favorable to the presence of Li_2O Schottky defects. The strength of the Coulombic A–O interactions is the source of such strong binding energies.[5]

Following the MD protocol described in the ESI† and in detail in ref. 5, the transport properties of the pristine $Li_{2-x}SiO_{3-0.5x}$, and doped $Li_{2-x}Na_xSiO_{3-0.5x}$ and $Li_{2-x}K_xSiO_{3-0.5x}$ samples were further studied. Fig. S3 (ESI†) displays the temporal evolution of the MSDs of the Li-ion in $Li_{2-x}SiO_{3-0.5x}$, $Li_{2-x}Na_xSiO_{3-0.5x}$ and $Li_{2-x}K_xSiO_{3-0.5x}$ at different temperatures and defect concentrations (x). All MSDs increase linearly with time, which indicates favorable Li-ion migration within Li_2SiO_3 structures. In the case of Na- and K-doped samples, reduction of Li-ion diffusion for the majority of dopant concentrations is observed, except for x = 0.06, where Li-ion diffusion is considerably improved. Besides, Na- or K-ion diffusion is lower than the Li counterpart in $Li_{2-x}Na_xSiO_{3-0.5x}$ and $Li_{2-x}K_xSiO_{3-0.5x}$ systems.[5]

Fig. 3(a)–(e) show the Arrhenius dependence of Li-ion diffusion for each system. At concentrations of x = 0.02 and 0.06, the Na-doped sample exhibits higher Li-ion diffusion than the pristine sample; while at x = 0.06 the K-doped sample has higher Li-ion diffusion as compared with the pristine sample. The calculated activation energies (denoted as E_a) range between 0.3 and 0.6 eV,[5] in agreement with previous findings.[34] The Na-doped sample has the lowest E_a value of 0.3 eV at a defect concentration of 0.02. This value is lower than others calculated for similar compounds, showing the potential of this composition as a solid-state electrolyte for alkali-ion batteries. The K-doped sample has

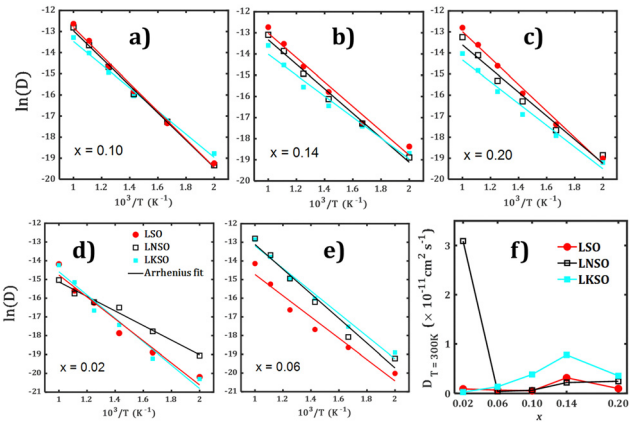

Fig. 3 (a)–(e) Arrhenius-type plots for Li-ion diffusion in $Li_{2-x}SiO_{3-0.5x}$ (LSO), $Li_{2-x}Na_xSiO_{3-0.5x}$ (LNSO) and $Li_{2-x}Na_xSiO_{3-0.5x}$ (LKSO) as a function of the dopant concentration (x). (f) Dependence of the Li-ion diffusion coefficient with respect to the dopant concentration (x) at 300 K.

the lowest E_a at a defect concentration x = 0.14. For the pristine sample upon defect concentration change, the corresponding activation energies are practically constant ($\approx$0.5 eV).[5]

Fig. 3(f) shows the diffusion coefficients of these systems at 300 K extrapolated from the previous Arrhenius fit. As is shown in Fig. 3(f), the highest diffusion coefficient is obtained for the Na-doped sample with x = 0.02. The influence of Na-doping on Li-ion diffusion is not significant at higher Na concentrations in the $Li_{2-x}Na_xSiO_{3-0.5x}$ system. Besides, the K-doped sample results in a higher Li-ion diffusion coefficient at higher dopant concentrations ($x > 0.06$). In this sense, Na-doping at low and K-doping at high dopant/defect concentrations can be used to improve the Li-ion transport of Li_2SiO_3, thus encouraging further experimental verifications and application as a solid-state electrolyte for current or future rechargeable alkali-ion batteries.

3.3 Disclosing the lithium and sodium ion migration in $Li_2Ti_6O_{13}$, $Na_2Ti_6O_{13}$ and $Li_2Sn_6O_{13}$ structures with the aid of NEB computations

Of particular interest, the migration path of the Li^+ and Na^+ ions in the $Li_2Ti_6O_{13}$, $Na_2Ti_6O_{13}$ and $Li_2Sn_6O_{13}$ compounds were explored using NEB computations, disclosing their capability to act as anode materials for alkali-ion batteries. The potential-based method is applied using force field parameters discussed in ref. 1 and 22 was adopted to model the pair ion interactions in $Li_2Ti_6O_{13}$, $Na_2Ti_6O_{13}$ and $Li_2Sn_6O_{13}$ structures. Supercells of 2 × 3 × 2-unit cells of $Li_2Ti_6O_{13}$, $Li_2Sn_6O_{13}$ and $Na_2Ti_6O_{13}$ were selected to create the initial, final and replica (image) structures. Fig. 4(a) displays the conventional representation of $Li_2Ti_6O_{13}$, $Li_2Sn_6O_{13}$ and $Na_2Ti_6O_{13}$, a scheme of the $[AO_4]$ (A = Li, Na, K) channel of the initial and final structures is depicted in Fig. 4(b). Two main incorporation mechanisms involving alkali substitution, and alkali and oxygen vacancies were considered for defect engineering in the host $Li_2Ti_6O_{13}$, $Na_2Ti_6O_{13}$ and $Li_2Sn_6O_{13}$ lattice structures.

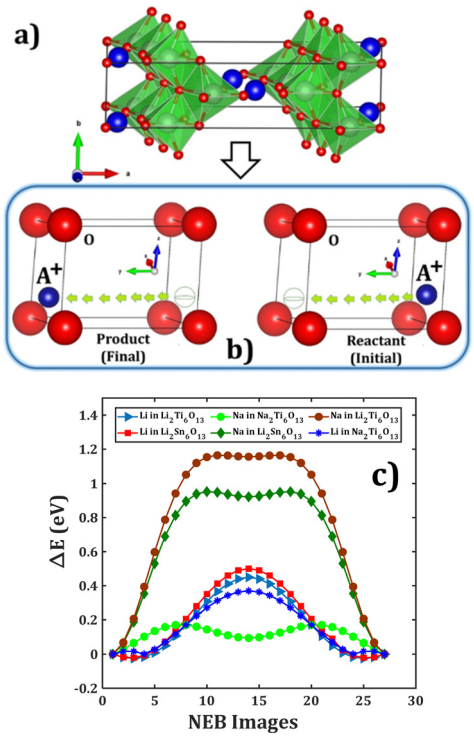

Fig. 4 (a) $Li_2Ti_6O_{13}$, $Li_2Sn_6O_{13}$ and $Na_2Ti_6O_{13}$ lattice structures, green polyhedra represent the TiO_6/SnO_6 octahedra, blue and red balls represent the A^+ (Li^+ or Na^+) and O ions, respectively, (b) initial and final structures for NEB and Sync calculations of the [AO_8] channel, and (c) energy profiles obtained by NEB computations.

From the results of defect energetics computations, we found that the energy of an alkali vacancy creation is lower for Na in $Na_2Ti_6O_{13}$ as compared to the Li vacancy in the Li-containing counterpart.[2] The Na substitution energy in $Na_2Ti_6O_{13}$ is negative, revealing the good Li storage capability of $Na_2Ti_6O_{13}$.[2] The solution energies for Na substitution at the Li-site in $Li_2Ti_6O_{13}$ and $Li_2Sn_6O_{13}$ lattice structures, and Li at the Na-site in $Na_2Ti_6O_{13}$ are negative, inferring that these compounds do not accept this modification without a significant structural change as a consequence.[2]

The results of NEB calculations of Li and Na migration of $Li_2Ti_6O_{13}$, $Li_2Sn_6O_{13}$ and $Na_2Ti_6O_{13}$ are shown in Fig. 4(c). The computed energy barriers (E_a) are 0.47 and 0.52 eV for Li migration in $Li_2Ti_6O_{13}$ and $Li_2Sn_6O_{13}$ structures, respectively. These values are smaller than those previously reported for other Li and Na containing compounds.[2,35] Concerning Li migration, the energy barrier is smaller in $Li_2Ti_6O_{13}$, which is attributed to the shorter Li–Li jump distance through the [LiO_8] channel.[2,26–28] The small difference in E_a values reveals that $Li_2Sn_6O_{13}$ is a potential anode candidate.

The most effective alkali diffusion corresponds to Li migration in $Na_2Ti_6O_{13}$ with the lowest energy barrier (0.4 eV), followed by Na migration in $Li_2Sn_6O_{13}$ and $Li_2Ti_6O_{13}$. Experimental studies explained a mechanism for Li insertion, which involves Ti^{4+} to Ti^{3+} reduction.[36,37] In our case, Ti^{4+} reduction is not considered as an incorporation mechanism and neutrality scheme.[2]

The $Na_2Ti_6O_{13}$ structure has potential transport properties for the anode in Li-ion batteries due to its better Li diffusion, in line with previous reports regarding Li insertion into the $Na_2Ti_6O_{13}$ anode.[26–28] Values of Na and Li migration in $Na_2Ti_6O_{13}$ point out the difference in diffusivity of four orders of magnitude higher for Na^+-migration.[2] This is also in line with the report of fast Na and low Li diffusion in the $Na_2Ti_6O_{13}$ structure.[37] The presence of multiple transition state structures can be the source of the performance deterioration as anodes of these compounds.[2] The influence of such pseudo-transition state structures on transport properties is discussed in detail in ref. 2.

3.4 Exploring the underutilized potential of strontium stannate as an anode for alkali-ion batteries with the aid of DFT and MD simulation computations

The strontium stannate material (denoted as $SrSnO_3$ or SSO) is involved in many technological applications.[38–40] Concerning its application in batteries, SSO has been studied experimentally as an anode,[39,40] but the lithiation/delithiation mechanism remains unresolved. Fig. 5(a) displays a conspectus of this section. Advanced atomistic simulations were performed to investigate the electronic properties and migration in alkali-doped SSO disclosing the influence of alkali ion inclusion on the electronic structure and alkali transport properties of mono- and polycrystalline SSO. Defect energetics computations were performed in considering the incorporation mechanism involving A^+ interstitial and Sr-vacancy as predominant point defects.[8,9]

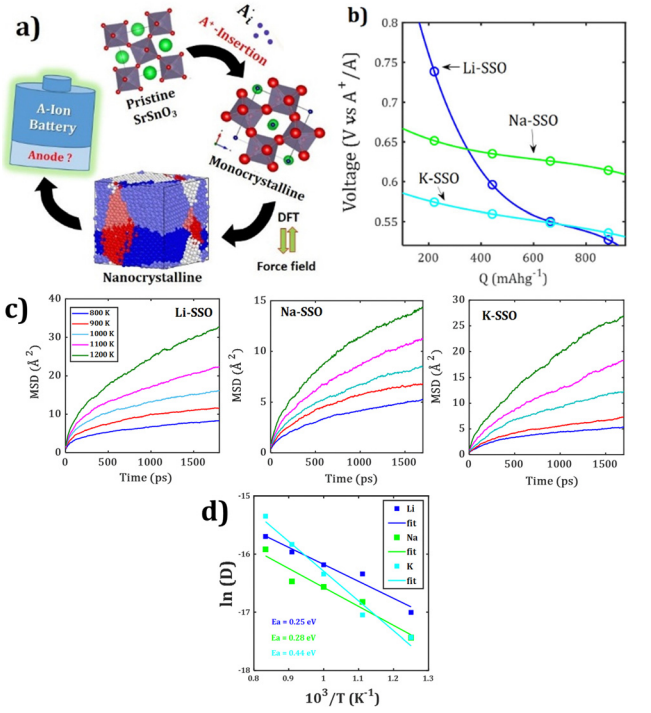

Fig. 5 (a) Research workflow used in ref. 8 and 9. (b) Discharge voltage/capacity profile of A^+ doped $SrSnO_3$ (A = Li^+, Na^+, K^+). A-SSO denotes Li-, Na- and K-doped $SrSnO_3$. (c) Temporal evolution of MSD at each temperature in nanocrystalline A-SSO samples, and (d) Arrhenius plots of diffusion coefficient (D) for A-SSO samples.

The results of defect energetics computations point out that the SSO structure accepts the inclusion of A^+ interstitially with a low energetic cost. In addition, the trapping effect of the Sr-vacancy of alkali-ions is reported.[8,9] From the results of defect energetics computations, the alkali interstitial mechanism allows the reactivity of the alkali ion with the SSO host structure to be explained, with consequences on the performance of SSO as anode.[8,9]

Commonly the SSO anode operates mainly in two steps; firstly by a conversion and secondly by an alloying/dealloying process.[39–41] A proposal for a complete set of first discharge reactions for SSO anode, where the A^+ interstitial mechanism is involved, was discussed in ref. 8 and 9. Fig. 5(b) shows the evolution profile of open cell voltage *vs.* theoretical capacity of A-SSO samples in which the common slope and plateau profiles in this anode material are observed in experiments employing SSO as anode for Li-ion batteries.[39,40] During the discharge progress, the Li-SSO shows the highest voltage variation. The plateau region for Na-SSO is observed at ≈ 0.6 V, while those for Li- and K-ions appear at ≈ 0.5 V. These low voltage values make the SSO compound quite suitable as an anode in alkali-ion batteries. In addition, our detailed description (disseminated in ref. 9) can be used to explain the unexpected high capacity of SSO nanorods, by estimating the amount of alkali-ions in the sample.[9,39,40]

Fig. 5(c) displays the of MSD plot *versus* simulation time for A^+-ions in nanocrystalline SSO at different temperatures. A monotonic increase of the MSD is observed upon temperature change. In comparison to Li-diffusion, both Na- and K-migrations are discreetly lower (*cf.* Fig. 5(d)), which is attributed to their larger ionic radius and heavier molar mass. The calculated E_a values for Li-, Na- and K-SSO samples point out that Li-doped samples have better transport properties.[9] While the transport properties are improved by the Li and Na interstitial incorporation mechanism, K-doping is less promising.[9]

The predicted values of diffusion coefficient at ambient temperature are similar to other anode materials used in alkali-ion batteries.[8,9] Considering the high capacity, low open cell voltage, and low diffusion barrier, the SSO compound represents a potential candidate for anode in Na-ion batteries, but again, less promising for K-ion batteries.

3.5 Static and molecular dynamics simulations providing doping strategies for improving the transport properties of Li_2SnO_3

Lithium stannate (Li_2SnO_3) is currently considered for many energy storage applications, including solid-state electrolyte, electrode and coating material in Li-ion batteries. By combining static and large-scale MD simulation, transition metal and divalent-doped Li_2SnO_3 derivatives were discussed in terms of transport properties, providing doping strategies to enhance the transport properties of this material.[6,7]

In order to disclose the transport properties, we studied various incorporation mechanisms: (a) Li_2O Schottky defect in undoped Li_2SnO_3, (b) divalent dopant (M^{2+}) at the Li-site with Li-vacancy formation $\left(M_{Li}^{\bullet} - V'_{Li}\right)$, and (c) substitution of M^{2+} at the Sn-site leading oxygen vacancy $\left(M''_{Sn} - V_O^{\bullet\bullet}\right)$. In addition, for trivalent dopants (M^{3+}), various defect reaction equations were considered.[6,7]

The solution, binding and final solution energies (E_s, E_B and E_f, respectively) were computed accordingly following the defect energetics protocol. Fig. 6(a) shows the results of E_s, E_B and E_f of each dopant. The formation energy of Li_2O Schottky defects is 2.0 eV per defect, close to the reported values in previous works.[6,7,42]

The E_s value varies from 1.8 to 2.8 eV per dopant for M^{2+} at the Li-site giving rise to a Li-vacancy as a compensation/incorporation scheme. The Cd^{2+}, Sc^{2+} and Mn^{2+} dopants have the lowest E_s and E_f values. In this direction, the Cd^{2+}, Sc^{2+} and Mn^{2+} dopants are favorable in controlling the Li-vacancy concentration in the sample with favorable energetic cost. All binding energies are negative, showing the effective formation of defect clusters within the incorporation mechanisms considered.

The introduction of a divalent dopant at the Li-site generates strong attractive interactions, while the interaction becomes even stronger for $M''_{Sn} - V_O^{\bullet\bullet}$ pairwise. For divalent dopants, Zn^{2+}, Fe^{2+} and Co^{2+} emerge as the best dopants controlling the oxygen vacancy concentration, whereas Sc^{2+} and Cd^{2+} are more appropriate for fine tuning the Li-vacancy concentration in M^{2+}-doped Li_2SnO_3 samples. Fig. 6(b) shows the defect energetic behavior for transition metal dopant, specifically for the 3+ charge state. The Li-interstitial mechanism has lower E_s and E_f values, suggesting that the Sn-site with Li-interstitial charge compensation is the preferential incorporation mechanism for trivalent dopants. Binding energies for trivalent dopants are similar to those discussed above for divalent dopants.

The Li-transport properties of doped Li_2SnO_3 samples were evaluated.[6,7] Fig. 6(c) shows the Arrhenius dependence of both dc-conductivity and diffusion coefficient for divalent doped Li_2SnO_3 samples. For divalent dopants (Sc^{2+}, Zn^{2+}, Cd^{2+} and Eu^{2+}), the dc-conductivity (σ) values were derived from the diffusion coefficient by using the Nernst–Einstein transformation.[7] Li-transport properties were evaluated for both mono- and nanocrystalline Li_2SnO_3 divalent-doped samples.[7] In monocrystalline divalent-doped Li_2SnO_3, all studied dopants tend to improve the Li-transport properties with low activation energies and diffusion/conduction of more than one order of magnitude, as compared to the undoped Li_2SnO_3 case.[7] The activation energy is calculated to amount to between 0.40–0.44 eV for diffusion and 0.34–0.38 eV for conduction. In monocrystalline divalent-doped Li_2SnO_3, Zn^{2+} is the best candidate for enhancement of transport properties. A reduction of the activation energy to 0.39–0.43 and 0.33–0.36 eV for diffusion and conduction, respectively, is detected in their polycrystalline counterparts. Besides, activation energies are smaller in polycrystalline samples, except for the nanocrystalline Zn^{2+} doped sample.[7] Consequently, the Li-ion transport properties can successfully be improved by doping with divalent dopants, leading to a better battery performance of polycrystalline samples.[6,7]

In the case of transition metal dopants, our results pointed out that the Li-diffusion coefficient is higher by one or two

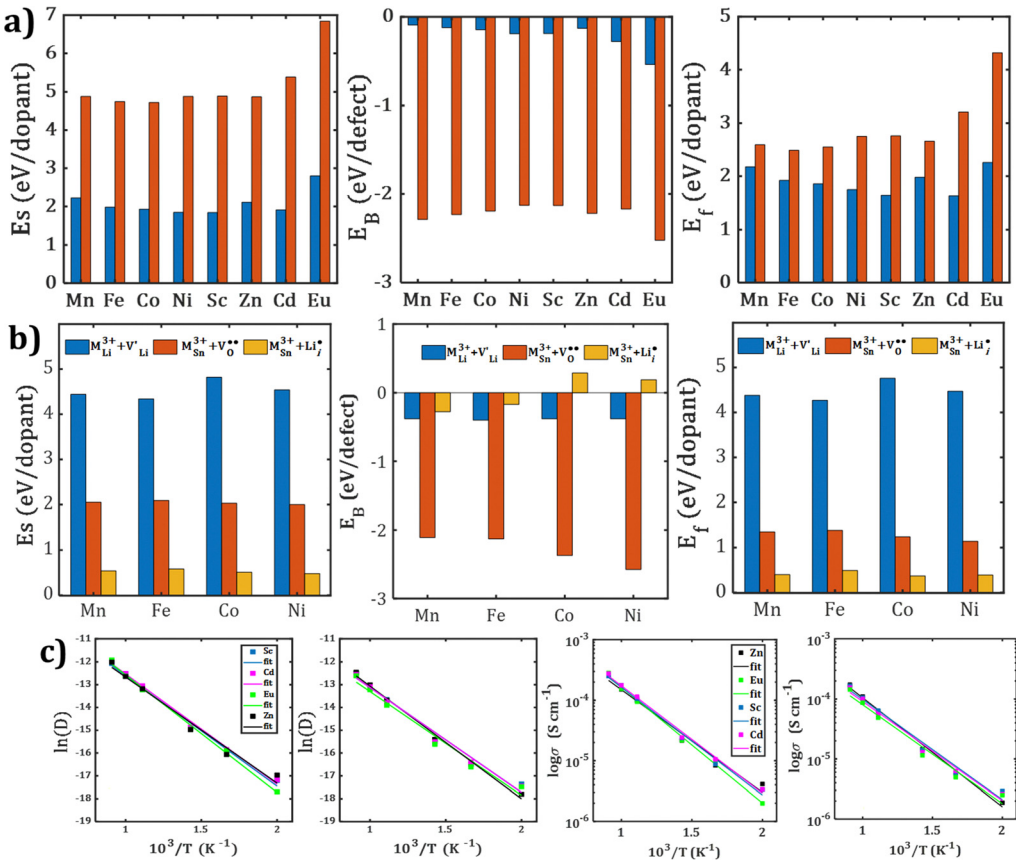

Fig. 6 Solution (E_s), binding (E_B) and final solution (E_f) energy of (a) (brown blocks) M^{2+} at Sn-site with an oxygen vacancy and (blue blocks) M^{2+} at a Li-site leading a Li-vacancy compensation mechanism, respectively. (b) E_s, E_B and E_f for transition metal dopant incorporation schemes, and (c) Arrhenius plot of Li-ion diffusion coefficient (D) and dc-conductivity (σ) of mono- and polycrystalline M^{2+}-doped Li_2SnO_3 samples, respectively.

orders of magnitude as compared to the undoped Li_2SnO_3, where the Li-interstitial scheme is involved.[6] The reduction of the average Li–Li distance constitutes the source of such improvements in transport properties, reducing the activation energy and alleviating Li-migration. As Mn^{3+} and Co^{3+} dopants have the lowest E_a with respect to the charge state and relatively low E_f, they can be considered for improvement of the transport properties in transition metal doped Li_2SnO_3 samples.[6] Furthermore, the inclusion of transition metal and pure divalent dopant into the Li_2SnO_3 structure effectively improves the quality of transport properties of Li_2SnO_3 with direct improvement for electrode/electrolyte in alkali-ion batteries.[6,7]

3.6 Transport properties of alkali–halide oxides A_3OX (A = Li, Na, X = Cl, Br) nanocrystalline samples by MD simulations

The Li-rich antiperovskite Li_3OX (X = Cl^-, Br^-) has attracted much scientific interest as an inorganic electrolyte.[43–45] In mixed anionic samples such as $Li_3OCl_{1-y}Br_y$ and $Li_{3-x}Na_xOCl_{1-y}Br_y$, the Cl/Br mixing has an irrelevant contribution to the conducting properties, but these doping strategies can be considered for gauging their transport properties.[43–48] In earlier studies the explicit influence of the grain boundaries on the transport properties in polycrystalline A_3OX samples was discussed, but this needs further revision.[45,46] High density of $\sum 3$ grain boundary type is expected to appear in real polycrystalline samples due to their low formation energy.[45,46]

By using large scale MD computations, we disclosed the transport properties of nanocrystalline A_3OX (A = Li, Na, X = Cl, Br) samples with the presence of $\sum 3(111)$ grain boundaries. Following the coincidence site theory,[45,48] the symmetric tilt $\sum 3(111)$ grain boundary was constructed from the A_3OX (A = Li^+, Na^+, X = Cl^-, Br^- in an ionic form) unit cell structures (see Fig. 7a).

We used the $\sum 3(111)$ grain boundary as the seed, applying the Voronoi tessellation method for generating the nanocrystalline A_3OX simulation boxes of 80 × 80 × 80 $Å^3$. These nanocrystals contain three grains connected with $\sum 3(111)$ grain boundaries.[10] The migration mechanism considered involves the A^+- and X^--vacancies forming an alkali-halide Schottky defect in these structures, facilitating the alkali migration.[10] Fig. 7(b) and 7(c) show the results of the stransport properties of A_3OX, Li_2NaOX and Na_2LiOX compounds. From the activation energies given in Fig. 7(b), Na_3OBr appears to have better transport properties with low activation energy for both conduction (E_a^σ) and diffusion (E_a^D), and with higher conductivity at ambient temperature.[10]

The results collected in ref. 10 disseminate the effect of grain boundary on the transport properties in these nanocrystalline

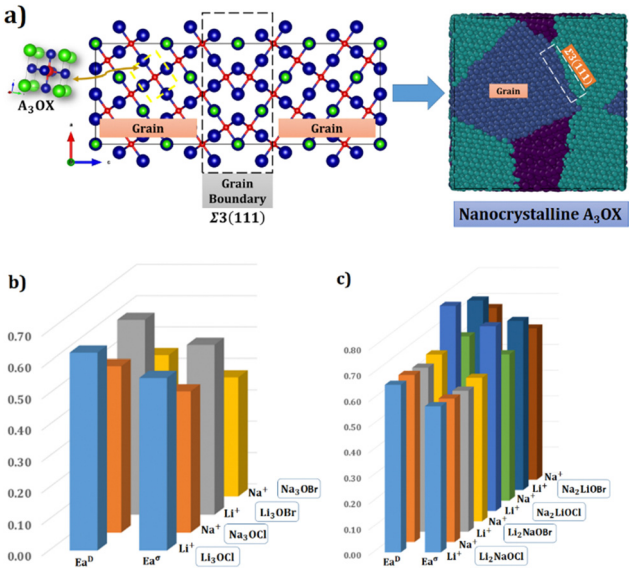

Fig. 7 (a) Outline of alkali-halide oxides A_3OX (A = Li, Na, X = Cl, Br) nanocrystalline samples in the presence of $\sum 3(111)$ grain boundaries. Activation energy (in eV) for Li- and Na-diffusion (E_a^D) and conduction (E_a^σ) of (b) A_3OX and (c) Li_2NaOX and Na_2LiOX compounds.

samples.[10] The magnitude of the conductivity agrees with the available experimental findings.[10,45,46,48] In this sense, our computed results are not only consistent with previous findings, but also explicitly explain how the presence of the $\sum 3(111)$ causes the high grain boundary resistance affecting the transport properties in real samples.[10,45]

The Li_2NaOX nanocrystals have the lowest activation energies for both charge and mass transport processes (see Fig. 7(c)). The Na-conductivity at 300 K of 10^{-7} S cm^{-1} for conduction in Li_2NaOCl nanocrystal is in good agreement with reports in the pristine Na_3OCl.[10,43,45,46] In the case of the other mixed alkali bromide Li_2NaOBr nanocrystal, we found that the Li- and Na- conductivity at 300 K is in the order of 8×10^{-8} S cm^{-1}.[10] The Na^+ conduction induces improvements in transport properties in Na_2LiOX nanocrystals. Comparing the Na_2LiOX nanocrystals, the Na_2LiOCl has better Na-transport properties instead of Li-migration.[10]

Analysis of the trajectory density map is a powerful tool to elucidate the dimensionality (1D, 2D and 3D) of alkali migration within a lattice structure.[7,10,45,46] The 3D characteristics of alkali-ion migration are confirmed from the analysis of the trajectory density map.[10] Data concerning trajectory density maps are given in the ESI† file (see Fig. S4 and S5). There is observable evidence for the grain resistance with high density maps near the grain boundaries.

In summary, large-scale molecular dynamic simulations show that the nanocrystalline alkali-ion mixed halides–bromides exhibit higher activation energies for transport processes as compared to previous theoretical computations,[10,43–45] and the activation energies found to lie much closer to the experimental data. This can be attributed to the introduction in our model of higher atomic density at the $\sum 3(111)$ grain boundaries. Despite some observations for deterioration of transport properties in mixed alkali halide–bromide samples (Li_2NaOX and Na_2LiOX), they can still be considered as alternative solid-state electrolytes in both Li- and Na-ion batteries.

4. Concluding remarks

In this Perspective, we have presented a set of practical theoretical protocols based on density functional theory, and static and large-scale molecular dynamics computations to determine the main properties of battery materials. These computational protocols allowed the exploration and prediction of their structural and electronic properties, together with a determination of the open cell voltage, thermodynamic stability and transport properties.

Of particular interest, a set of new compounds have been proposed by using cation and/or anion substitution in $A_2B_6X_{13}$ (A = Li^+, Na^+ or K^+; B = Ti^{4+} or Sn^{4+}; X = O^{2-} or S^{2-}) structures. Such a substitution is based on experimental backgrounds concerning the ion exchange method. Following DFT protocols presented throughout the sections, exploration of the structural, electronic and thermal stability of the $A_2B_6S_{13}$ and $A_2B_6O_{13}$ structures disclose that the sulfur derivatives have larger lattice parameters, better electronic structures and stability as compared to their oxygen counterparts. The potential application of the $A_2B_6X_{13}$ compounds including A = Li^+, Na^+ or K^+; B = Ti^{4+} or Sn^{4+}; X = O^{2-} or S^{2-} as an anode/electrolyte can now be presented to the experimental community.

Defect chemistry and MD simulations allowed us to propose the silicate Li_2SiO_3 compound as a potential material for solid-state lithium batteries. Static simulations based on combined nudged elastic band computations were carried out for an understanding of the Li- and Na-ion migration process of $Li_2Ti_6O_{13}$, $Li_2Sn_6O_{13}$ and $Na_2Ti_6O_{13}$. Calculated results emphasized the presence of quasi-transition state structures lowering the energy barriers of Na^+- and Li^+-ion migrations in $Na_2Ti_6O_{13}$ electrode.

DFT computations, together with MD simulations and defect energetic analysis, revealed the underutilized potential of $SrSnO_3$ as an anode for alkali-ion batteries. Trivalent/divalent doping emerges as an improvement of the transport properties of Li_2SnO_3, highlighting the substantial enhancement of the Li-ion migration in this compound. The influence of $\sum 3(111)$ grain boundaries on the transport properties of A_3OX nanocrystals was also discussed. These polycrystalline samples are characterized by higher activation energies as compared to values reported in previous theoretical studies, but much closer to the experimental data, which is attributed to the higher density at the $\sum 3(111)$ grain boundaries considered in our model. The Na_3OBr is a promising compound for solid-state electrolytes in Na-ion batteries technologies. In addition, mixed alkali halides–bromides nanocrystals (Li_2NaOX and Na_2LiOX) can also be considered as inorganic solid-state electrolytes for both Li- and Na-ion batteries.

Remarks concerning the advantages and disadvantages inherently associated with the computational protocols were presented by means of many specific examples presented in

this manuscript. For instance, the DFT method is good for relatively small systems, but it is necessary to use various exchange–correlation functionals. The intrinsic underestimation problem needs also to be examined carefully. For force field-based computations, the selection of the force field is another crucial criterion to be considered. While the NEB computation is good for a rapid prediction of transport properties, large–scale MD computations are more appropriate to consider explicitly the temperature dependence of the structural and transport properties of the compounds considered. For the NEB and synchronous transition state computations, the selection of initial and final structures, together with the number of replicas connecting the reactant and product in a hypothetical reaction, as well as the spring constant, are of vital importance for confident prediction of transition state structure and transport properties.

To perform more accurate MD computations, it is necessary to first perform an equilibration and relaxation with periodic boundary conditions to ensure that the thermodynamic equilibrium of the system is reached. For the production run the use of the *NVT* ensemble is needed to avoid the volume change in order to obtain reasonable diffusion data.

The theoretical protocols presented and discussed in the sections can, in principle, be applied to other types of solid-state compounds to predict, with reasonable accuracy, their properties related to their possible applications as battery materials.

Conflicts of interest

There are no conflicts to declare.

Acknowledgements

The work of MTN is funded by VinGroup (Vietnam) and supported by VinGroup Innovation Foundation (VinIF) under project code VinIF.2020.DA21; he is also grateful to Van Lang University. We thank Profs. Paul Geerlings and Frederik Tielens (Vrije Universiteit Brussel, Belgium), Dr James A. Dawson (Newcastle University, UK), and Prof. Mathy Froeyen (KU Leuven, Belgium) for enjoyable cooperation. YAZ thanks Mr Bjorn Jahnsen for his language review and valuable proposals for improvements.

Notes and references

1 Y. A. Zulueta and M. T. Nguyen, *Phys. Status Solidi B*, 2018, **255**, 1–9.
2 Y. A. Zulueta, P. Geerlings, F. Tielens and M. T. Nguyen, *J. Solid State Chem.*, 2019, **279**, 120930.
3 Y. A. Zulueta Leyva and M. T. Nguyen, *Phys. Status Solidi B*, 2019, **256**, 1800568.
4 Y. A. Zulueta, P. Geerlings, F. Tielens and M. T. Nguyen, *J. Phys. Chem. C*, 2019, **123**, 24375–24382.
5 Y. A. Zulueta, M. T. Nguyen and J. A. Dawson, *J. Phys. Chem. C*, 2020, **124**, 4982–4988.
6 Y. A. Zulueta, M. T. Nguyen and J. A. Dawson, *Inorg. Chem.*, 2020, **59**, 11841–11846.
7 Y. A. Zulueta and M. T. Nguyen, *Dalton Trans.*, 2021, **50**, 3020–3026.
8 Y. A. Zulueta, R. Mut, S. Kaya, J. A. Dawson and M. T. Nguyen, *J. Phys. Chem. C*, 2021, **125**, 14947–14956.
9 Y. A. Zulueta, M. T. Nguyen and M. P. Pham-Ho, *J. Phys. Chem. Solids*, 2022, **162**, 110505.
10 L. Van Duong, M. T. Nguyen and Y. A. Zulueta, *RSC Adv.*, 2022, **12**, 20029–20036.
11 Z. Ding, J. Li, J. Li and C. An, *J. Electrochem. Soc.*, 2020, **167**, 70541.
12 M. S. Whittingham, *Chem. Rev.*, 2004, **104**, 4271–4301.
13 A. Ahniyaz, I. de Meatza, A. Kvasha, O. Garcia-Calvo, I. Ahmed, M. F. Sgroi, M. Giuliano, M. Dotoli, M.-A. Dumitrescu, M. Jahn and N. Zhang, *Adv. Appl. Energy*, 2021, **4**, 100070.
14 J. Zheng, Y. Wu, Y. Sun, J. Rong, H. Li and L. Niu, *Nano-Micro Lett.*, 2021, **13**, 1–37.
15 T. F. Yi, T. T. Wei, Y. Li, Y. B. He and Z. B. Wang, *Energy Storage Mater.*, 2020, **26**, 165–197.
16 H. Tian, F. Xin, X. Wang, W. He and W. Han, *J. Mater.*, 2015, **1**, 153–169.
17 T. D. H. Nguyen, H. D. Pham, S. Y. Lin and M. F. Lin, *RSC Adv.*, 2020, **10**, 14071–14079.
18 Z. Zhang, L. Zhang, X. Yan, H. Wang, Y. Liu, C. Yu, X. Cao, L. van Eijck and B. Wen, *J. Power Sources*, 2019, **410–411**, 162–170.
19 A. Sakuda, A. Hayashi, Y. Takigawa, K. Higashi and M. Tatsumisago, *J. Ceram. Soc. Jpn.*, 2013, **121**, 946–949.
20 W. Huang, N. Matsui, S. Hori, K. Suzuki, M. Hirayama, M. Yonemura, T. Saito, T. Kamiyama, Y. Sasaki, Y. Yoon, S. Kim and R. Kanno, *J. Am. Chem. Soc.*, 2022, **144**, 4989–4994.
21 J. A. Brant, D. M. Massi, N. A. W. Holzwarth, J. H. Macneil, A. P. Douvalis, T. Bakas, S. W. Martin, M. D. Gross and J. A. Aitken, *Chem. Mater.*, 2015, **27**, 189–196.
22 Y. A. Zulueta, M. Froeyen and M. T. Nguyen, *Comput. Mater. Sci.*, 2017, **136**, 271–279.
23 Y. A. Zulueta, J. A. Dawson, M. Froeyen and M. T. Nguyen, *Phys. Status Solidi B*, 2017, **254**, 1700108.
24 Z. E. Biskri, H. Rached, M. Bouchear and D. Rached, *J. Mech. Behav. Biomed. Mater.*, 2014, **32**, 345–350.
25 J. C. Pérez-Flores, F. García-Alvarado, M. Hoelzel, I. Sobrados, J. Sanz and A. Kuhn, *Dalton Trans.*, 2012, **41**, 14633–14642.
26 J. Kanchanawarin, W. Limphirat, P. Promchana, T. Sooknoi, T. Maluangnont, K. Simalaotao, A. Boonchun, P. Reunchan, S. Limpijumnong and J. T-Thienprasert, *J. Appl. Phys.*, 2018, **124**, 155101.
27 J. C. Pérez Flores, M. Hoelzel, A. Kuhn and F. García Alvarado, *ECS Trans.*, 2012, **41**, 195–206.
28 R. Dominko, L. Dupont, M. Gaberščček, J. Jamnik and E. Baudrin, *J. Power Sources*, 2007, **174**, 1172–1176.
29 J. Maier, *Z. Anorg. Allg. Chem.*, 2017, **643**, 2083–2087.
30 M. Shimizu, K. Kimoto, T. Kawai, T. Taishi and S. Arai, *ACS Appl. Energy Mater.*, 2021, **4**, 7922–7929.

31 N. Sarukura, T. Nawata, H. Ishibashi, M. Ishii and T. Fukuda, Czochralski growth of oxides and fluorides, in, *Handbook of Crystal Growth*, ed. P. Rudolph, Elsevier, Boston, MA, USA, 2nd edn, 2015, pp.131–168.
32 H. Kim, Y. W. Byeon, J. Wang, Y. Zhang, M. C. Scott, K. J. Jun, Z. Cai and Y. Sun, *Energy Storage Mater.*, 2022, **47**, 105–112.
33 S. Katayama, T. Katase, T. Tohei, B. Feng, Y. Ikuhara and H. Ohta, *Cryst. Growth Des.*, 2017, **17**, 1849–1853.
34 N. Kuganathan, L. H. Tsoukalas and A. Chroneos, *Solid State Ionics*, 2019, **335**, 61–66.
35 M. M. Islam, T. Bredow and P. Heitjans, *J. Phys.: Condens. Matter*, 2012, **24**, 203201.
36 P. Li, P. Wang, S. Qian, H. Yu, X. Lin, M. Shui, X. Zheng, N. Long and J. Shu, *Electrochim. Acta*, 2016, **187**, 46–54.
37 C. Ling and R. Zhang, *Phys. Chem. Chem. Phys.*, 2017, **19**, 10036–10041.
38 S. M. de Freitas, P. C. L. dos Santos and M. V. dos S. Rezende, *J. Solid State Chem.*, 2019, **279**, 120928.
39 X. Hu, Y. Tang, T. Xiao, J. Jiang, Z. Jia, D. Li, B. Li and L. Luo, *J. Phys. Chem. C*, 2010, **114**, 947–952.
40 C. Li, Y. Zhu, S. Fang, H. Wang, Y. Gui, L. Bi and R. Chen, *J. Phys. Chem. Solids*, 2011, **72**, 869–874.
41 F. Zoller, D. Böhm, T. Bein and D. Fattakhova-Rohlfing, *ChemSusChem*, 2019, **12**, 4140–4159.
42 N. Kuganathan, A. Kordatos and A. Chroneos, *Sci. Rep.*, 2018, **8**, 3–11.
43 A. Ahniyaz, I. de Meatza, A. Kvasha, O. Garcia-Calvo, I. Ahmed, M. F. Sgroi, M. Giuliano, M. Dotoli, M. A. Dumitrescu, M. Jahn and N. Zhang, *Adv. Appl. Energy*, 2021, **4**, 100070.
44 Z. Deng, B. Radhakrishnan and S. P. Ong, *Chem. Mater.*, 2015, **27**, 3749–3755.
45 J. A. Dawson, P. Canepa, T. Famprikis, C. Masquelier and M. Saiful Islam, *J. Am. Chem. Soc.*, 2017, **140**, 362–368.
46 J. Zhu, Y. Wang, S. Li, J. W. Howard, J. Neuefeind, Y. Ren, H. Wang, C. Liang, W. Yang, R. Zou, C. Jin and Y. Zhao, *Inorg. Chem.*, 2016, **55**, 5993–5998.
47 B. Chen, C. Xu and J. Zhou, *J. Electrochem. Soc.*, 2018, **165**, A3946–A3951.
48 H. H. Heenen, J. Voss, C. Scheurer, K. Reuter and A. C. Luntz, *J. Phys. Chem. Lett.*, 2019, **10**, 2264–2269.